Research Square

Preprints are preliminary reports that have not undergone peer review.
They should not be considered conclusive, used to inform clinical practice,
or referenced by the media as validated information.

Bearing Capacity Prediction of Lightweight Steel Double L-Joints Based on Experimental Investigation and an Improved Gaussian Process Regression Algorithm

Ding Wei
Guizhou University of Engineering Science
Jia Suizi
2016010023@cugb.edu.cn
China University of Geosciences (Beijing)

Research Article

Keywords: Light steel frame, Beam–column joint area, Post-earthquake axial compression performance, GPR, Carrying capacity

Posted Date: March 4th, 2026

DOI: https://doi.org/10.21203/rs.3.rs-8811407/v1

License: This work is licensed under a Creative Commons Attribution 4.0 International License.
Read Full License

Additional Declarations: No competing interests reported.

Bearing Capacity Prediction of Lightweight Steel Double L-Joints Based on Experimental Investigation and an Improved Gaussian Process Regression Algorithm

Ding Wei[1,3], Jia Suizi[2], *

1 Guizhou University of Engineering Science, No. 1 Xueyuan Road, Qixingguan District, Bijie City, Guizhou Province, 551700, China

2 School of Engineering and Technology, China University of Geosciences (Beijing), No. 29, Xueyuan Road, Haidian District, Beijing 100083, China

3 Key Laboratory of Intelligent Monitoring of Bridges in Mountainous Areas of Bijie City.

Corresponding author: Jia Suiz

Abstract: The vertical load-bearing capacity of earthquake-damaged prefabricated frame structures determines their ability to resist collapse during aftershocks. In particular, the response performance of the beam-column joint area of prefabricated frame structures to axial compression after earthquake damage plays a key role in determining the vertical load-bearing capacity of the structure. To study the bearing capacity of beam-column joints in post-earthquake prefabricated light steel frames, firstly, based on nine existing low-cycle repeated loading tests of beam-column joints in different structural prefabricated light steel frames, axial compression performance tests were conducted on nine joints with different degrees of damage and different structures by applying axial forces to the frame columns. The failure modes and bearing capacities of joints with different structures were compared. Secondly, the experimental structures were verified through numerical simulation, and a database was constructed based on experimental and finite element results. Finally, an improved particle swarm optimization algorithm was used to optimize GPR, and the IPSO-GPR algorithm was proposed to form a prediction method for the bearing capacity of light steel frame structures. The results show that the proposed bearing capacity prediction method can better reflect the stress characteristics of such specimens.

Keywords: Light steel frame; Beam–column joint area; Post-earthquake axial compression performance; GPR; Carrying capacity

1. Introduction

The 21st century has seen a rapid development of fabricated buildings. Fabricated building structures have the following benefits: reliable mechanical properties, short construction period, low construction costs, and relatively little construction waste[1-7]. The seismic performance of prefabricated building structures mainly depends on the main components, including beams, slabs, columns, walls, and their connecting joints. The seismic performance of prefabricated frame structures is determined by beams, columns, and beam–column joints. In aseismic design, such structures are required to have "strong columns, weak beams, and stronger joints", and the rational design of beam–column joints for prefabricated frames is particularly important[8-14]. In practical applications, bolted connections are often used as beam–column joints. Liu et al.[15], Li et al.[16], and Rajagopal et al.[17] have found that bolted connections are easy to assemble and disassemble and can improve the carrying capacity of the joint area. In addition to bolted connections, both tests and numerical simulations have shown that fabricated specimens with the joint area assembled by mixed joints[18-20] can improve the ductility and meet the design requirements of "strong joints and weak components".

At present, most studies on seismic performance of fabricated building joints[21-26] are based on the test for joint components under a main shock. The beam–column joint of the new cast steel connector proposed by Xue et al. has good seismic performance[27]. Zhang et al. proposed a new type of assembled buckling-restrained brace with an inner core and double yield points based on the requirement for "no collapse in major earthquakes"[28]. Wang[29] studied the fabricated buckling-restrained joint, with the results showing that this joint can significantly improve the seismic performance of the structure. In addition to new con-

struction forms, increasing the joint area and its stiffness and strength can also improve the seismic performance of beams and columns[30-35]. Yao et al.[36] proposed the addition of haunch boards at beam–column connections to increase the joint area. Guo et al.[37] studied the seismic performance of the cover-plate joint with external stiffening rings. The composite joint proposed by Ding et al.[38] showed good seismic performance in the energy-intensive composite wall structure test.

To investigate the load-bearing capacity of structures, researchers utilize machine learning for predicting concrete compressive strength [39], concrete fatigue strength [30], flexural strength of reinforced concrete beams [41], load-bearing capacity of reinforced concrete beam-columns [43], as well as structural response and performance [44-45]. Currently, a prevalent approach adopted by researchers is to train a surrogate model using machine learning, which can be utilized to simulate the structural response or mechanical properties observed in experiments. By inputting variables such as structural characteristics, load characteristics, and material properties into the surrogate model, one can obtain the structural response or mechanical performance indicators without resorting to intricate nonlinear time-history analysis, vulnerability analysis, or other computational procedures. However, machine learning methods often rely on extensive data to train predictive models. For lightweight steel frame structures, acquiring a substantial amount of experimental data is challenging due to the difficulties in conducting experiments, fabricating test specimens, and the high cost of experimentation. Therefore, analysis based on machine learning can only be conducted under the condition of small samples.

The vertical load-bearing capacity of prefabricated frame structures damaged in the main earthquake can control the seismic collapse performance of light steel frame structures. Currently, there is limited research on the post-earthquake vertical load-bearing capacity of light steel frame structures under small sample conditions. Therefore, this paper first conducted an axial compression performance test on nine beam-column joint specimens damaged in low-cycle repeated loading tests, which simulated the damage of components in the main earthquake. Secondly, numerical simulation was used to verify the test process and reproduce data, laying the foundation for subsequent machine learning research. Finally, the PSO algorithm was improved to optimize GPR, and the IPSO-GPR algorithm was proposed, forming a post-earthquake load-bearing capacity prediction method for light steel frames.

2. Test

2.1 Original specimens for the low-frequency cyclic loading tests

In the early stage, the research group carried out 9 groups of low cycle repeated load tests on members. reference [46] shows details.

The 9 full-size T-shaped frame beam–column joint specimens, including 4 control pieces, respectively 2 common bolted–welded joint specimens and 2 π-shaped bolted joint specimens (with concrete-filled steel tubular (CFST) or H-shaped steel columns, H-shaped steel beams, and π-shaped beam–column joints), and 5 double L-shaped bolted joint specimens with diagonal ribs (with CFST or H-shaped steel columns, H-shaped steel beams, and double L-shaped joints with diagonal ribs). The joint connection type, frame column type, column size, H-beam size, and joint construction of each specimen are shown in Table 1. To match the specimen with the loading device, 86-mm-high CFSTs with a cross section of 100 mm × 100 mm are set at the upper and lower ends of the column to insert into the end of the loading device. For the geometric dimensions of some specimens, see the literature[46].

The fabricated light steel frame beam–column joint specimen connected with high-strength bolts is composed of the following parts: square CFST or H-shaped steel column, π-shaped joint or double L-shaped joint with diagonal ribs welded onto the CFST column or the flange of the H-shaped steel column, web connecting plate welded onto the CFST or the flange of the H-shaped steel column, and H-shaped steel beam. In particular, the π-shaped connector is connected with the CFST column

through two rectangular closed welding seams on the inner and outer sides of the hollow square bottom plate, and the web connecting plate passes through the hole in the hollow square bottom plate to be welded to the steel tube wall.

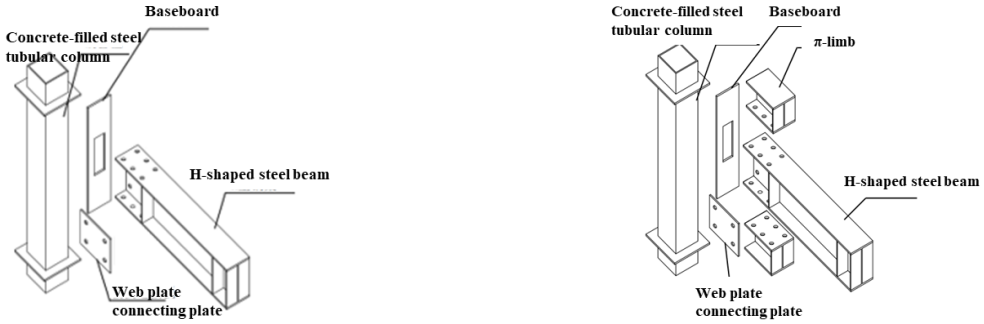
Table 1 Design Parameters of Specimens

Specimen No.	Joint Connection Type	Frame Column Type	Column Size	Size of H-shaped Steel Beam	Joint Construction
1	Bolted–welded joint	Square CFST column	120×120×5	150×120×5×8	Web connecting plate
2	Bolted–welded joint	H-shape steel column	150×120×5×8	150×120×5×8	Web connecting plate
π-1	π-shaped joint with diagonal stiffener	Square CFST column	120×120×5	150×120×5×8	π-shaped connector, with upper and lower limbs of 120 mm in length and bottom plate of 6 mm in thickness
π-2	π-shaped joint with diagonal stiffener	H-shape steel column	150×120×5×8	150×120×5×8	π-shaped connector, with upper and lower limbs of 120 mm in length and bottom plate of 6 mm in thickness
L-1	Double L-shaped joint with diagonal stiffener	Square CFST column	120×120×5	150×120×5×8	Double L-shaped connector with diagonal rib, with an L limb of 150 mm in length
L-2	Double L-shaped joint with diagonal stiffener	Square CFST column	120×120×5	150×120×5×8	Double L-shaped connector with diagonal rib, with an L limb of 200 mm in length
L-3	Double L-shaped joint with diagonal stiffener	H-shape steel column	150×120×4×6	150×120×5×8	Double L-shaped connector with diagonal rib, with an L limb of 150 mm in length
L-4	Double L-shaped joint with diagonal stiffener	H-shape steel column	150×120×5×8	150×120×4×6	Double L-shaped connector with diagonal rib, with an L limb of 150 mm in length
L-5	Double L-shaped joint with diagonal stiffener	H-shape steel column	150×120×5×8	150×120×5×8	Double L-shaped connector with diagonal rib, with an L limb of 150 mm in length

2.2 specimens

2.2.1 Control group specimens

The control group specimens include 2 common bolted–welded joint specimens and 2 π-shaped bolted joint specimens . The structural form of the control group specimen is shown in Figure 1

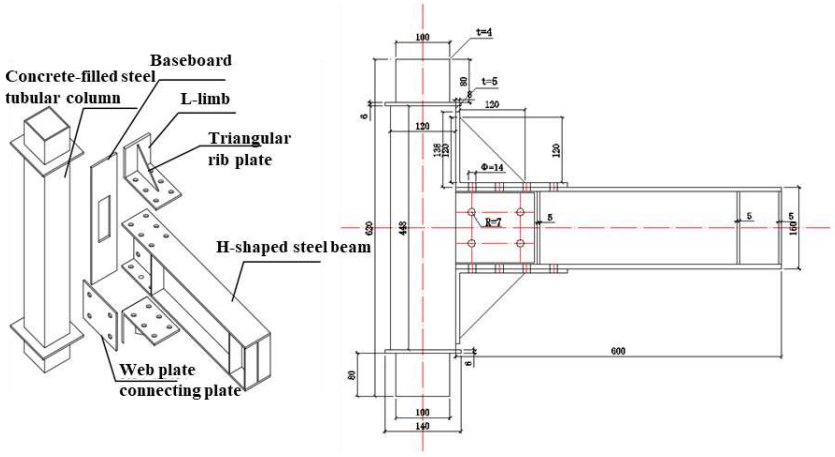


(a) Bolted–welded joints of CFST column and H-shaped steel column (b) π -shaped joints of CFST column and H-shaped steel column

Figure 1 Control group specimens

2.2.2 Double L-shaped joint with diagonal rib

The constructions for typical double L-shaped beam–column joints with diagonal ribs of CFST columns and H-shaped steel columns are shown in Figure 2(a), and the construction and size of a typical double L-shaped beam–column joint specimen with diagonal rib of CFST column are shown in Figure 2(b)[46].



(a) Double L-shaped joints of CFST column and H-shaped steel column (b) Double L-shaped joint specimen of CFST column

Figure 2 Construction of Typical Double L-Shaped Beam–Column Joint Specimens with Diagonal Ribs of Light Steel Frame

2.3 Material properties

The mechanical property test is performed for the steel plates and high-strength bolts used in 9 specimens. Their measured mechanical properties are shown in Table 2. According to the table, fy is the yield strength of the steel plate (Mpa); ε_y is the yield strain of the steel plate, and the mean value of the measured yield strain ε_y of steel plates with different thicknesses is 0.0016; fu is the ultimate strength of the steel plate (Mpa); Es is the elastic modulus of the steel plate (Mpa); δ is the elongation of the steel plate (%); fv is the shear strength of the bolt (Mpa).

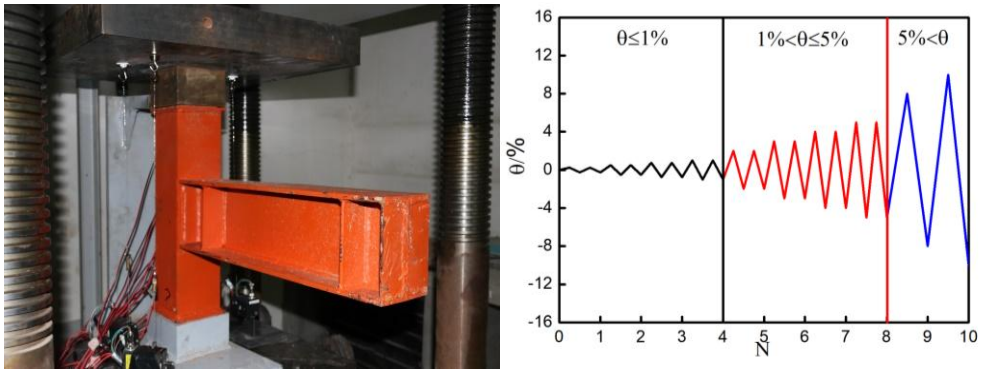
Table 2 Mechanical Properties of Steel Plates and High-strength Bolts

Steel	Type	f_y	ε_y	f_u	E_s	δ	f_v
Steel plate	t=4mm	368.67	510.33	205	20.17	--	t=4mm
	t=5mm	299.67	452.33	210	26.50	--	t=5mm
	t=6mm	316.33	467.67	210	26.77	--	t=6mm
	S8.8 M12	--	871.00	--	--	544.00	S8.8 M12
High-strength Bolt	t=4mm	368.67	510.33	205	20.17	--	t=4mm

2.4 Testing apparatus and loading system

In the axial compression performance test for beam–column joint area of the light steel frame, the universal tester WE-100 is used, and the maximum loading weight is 100 t. The loading device is shown in Figure 3(a). The low-frequency cyclic loading test process is shown in Figure 3(b)

The axial compression loading system used in this test first uses force to control loading and improve it at a speed of 3 kN/s to 400 kN. Damage to the specimen is observed after the load of 400 kN has been maintained for 20 s. Then, displacement is used to control loading to maintain the displacement rate at 2 mm/min until the specimen is obviously damaged and the loading can no longer continue or the carrying capacity falls below 85% of the peak load.



(a) Test device (b) Low-cycle loading system

Figure 3 Test Device and Loading system

2.5 strain gages arrangement

Six strain gages are arranged for each specimen, with three each on side A and side B of the specimen, to measure the development of axial strain at different positions of CFST column or H-shaped steel column webs and flanges. The arrangement of strain gages is shown in Figure 4.

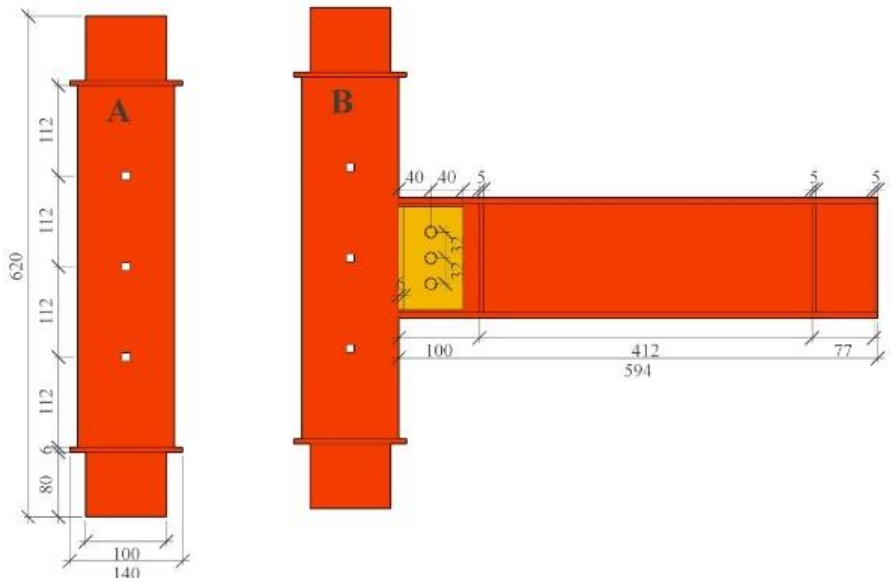


Figure 4 Arrangement of Specimen strain gages

3 Axial Compression Performance of Beam–Column Joint Area

3.1 Testing procedure under the axial compression loading tests

In order to gain a clearer understanding of the bearing capacity of 9 specimens under aftershocks, axial compression load loading tests were conducted on them.

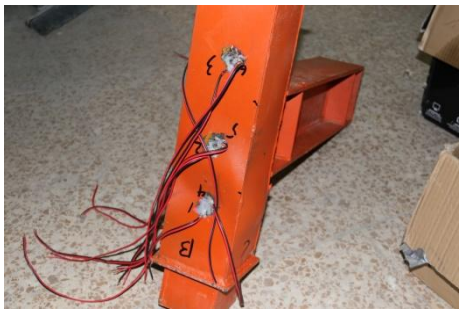
For the ease of describing the testing procedure, the two sides of the CFST column or H-shaped steel column closer to the beam end are called side A and side C, and that farther from the beam end is called side B,as shown in Figure 5 .Side A and side C are stressed symmetrically, and they suffer from similar damage and destruction. Thus, the specimen failure process mainly describes side A and side B. With the position at the top of the column being zero, the part facing downwards is positive to describe the damaged site.

(1) Control group specimens

Specimen 1: When loading to 400 kN, the joint area of the specimen is basically at the elastic stage. After the Specimen enters the plastic stage, the column wall at the upper end of the steel tube buckles, and the steel tube wall tears. During the loading process, brittle failure sounds are heard at the failure stage of the specimen. On side B, the depression at 152 mm is approximately 32 mm long, and the protrusion at 251 mm has a length of approximately 51 mm. On side A, the protrusion at 174 mm is approximately 68 mm long, and the depression at 237 mm has a length of approximately 28 mm. The damage and destruction on both side A and side B are within the joint area, as shown in Figure 5(a).

Specimen 2: Obvious damage is not observed at joint areas of the joint before loading. When loading to 400 kN, the joint area of the specimen is basically at the elastic stage, and after the Specimen enters the plastic phase, the upper and lower flanges

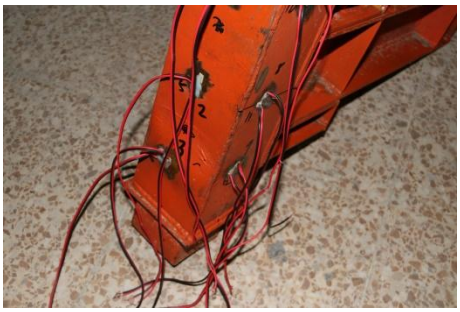
of the H-shaped steel column in the joint area buckle and suffer severe damage. The damage and destruction on both side A and side B are within the joint area, as shown in Figure 5(b).



(a) Specimen 1



(b) Specimen 2



(c) π-1



(d) π-2

Figure 5 Destruction of specimens

Specimen π-1: When loading to 450 kN, the joint area of the specimen is basically at the elastic stage. After the Specimen enters the plastic stage, the column wall at the upper end of the steel tube buckles, and the steel tube wall tears. Brittle failure sounds are heard when loading to 680 kN. The crack at 362 mm on side A expands from 112 mm to 117 mm in length, and the steel tube wall near the crack is depressed by 14 mm. For side B, the column surface at 412 mm bulges 49 mm outwards. No obvious damage is found in the beam–column junction in the joint area, as shown in Figure 5(c).

Specimen π-2: When loading to 450 kN, the joint area of the specimen is basically at the elastic stage, and after the Specimen enters the plastic phase, the lower flange of the H-shaped steel column buckles and suffers severe damage. No obvious damage is found in the beam–column junction in the joint area, as shown in Figure 5(d).

(2) Double L-shaped joint with diagonal rib

Specimen L-1: When loading to 450 kN, the joint area of the specimen is basically at the elastic stage. After the Specimen enters the plastic stage, the CFST column wall buckles, and the sealing seam on the CFST column wall cracks. Brittle failure sounds are heard once loaded to the plasticity rising stage. Side A bulges at 350-430 mm and is sunken at 430-510 mm. On side B, there is depression at 350-430 mm and protrusion at 430-500 mm. No obvious damage is found in the beam–column junction in the joint area, as shown in Figure 6(a).



(a) L-1 (b) L-2



(c) L-3 (d) L-4



(e) L-5

Figure 6 Destruction of specimens

Specimen L-2: When loading to 450 kN, the joint area of the specimen is basically at the elastic stage. After the Specimen enters the plastic stage, the CFST column wall buckles, and the sealing seam on the CFST column wall cracks. Side A bulges at 390-460 mm and is sunken at 460-500 mm. At the junction between side A and side B, no obvious damage is found in the beam–column junction in the joint area at 430 mm from the top of the column, as shown in Figure 6(b).

Specimen L-3: When loading to 450 kN, the joint area of the specimen is basically at the elastic stage, and after the Specimen enters the plastic phase, the lower flange of the H-shaped steel column buckles and suffers severe damage. No obvious damage is found in the beam–column junction in the joint area, as shown in Figure 6(c).

Specimen L-4: When loading to 450 kN, the joint area of the specimen is basically at the elastic stage, and after the Specimen enters the plastic phase, the upper flange of the H-shaped steel column buckles and suffers severe damage. No obvious damage is found in the beam–column junction in the joint area, as shown in Figure 6(d).

Specimen L-5: When loading to 450 kN, the joint area of the specimen is basically at the elastic stage, and after the Specimen enters the plastic phase, the upper flange of the H-shaped steel column buckles and suffers severe damage. No obvious damage is found in the beam–column junction in the joint area, as shown in Figure 6(e).

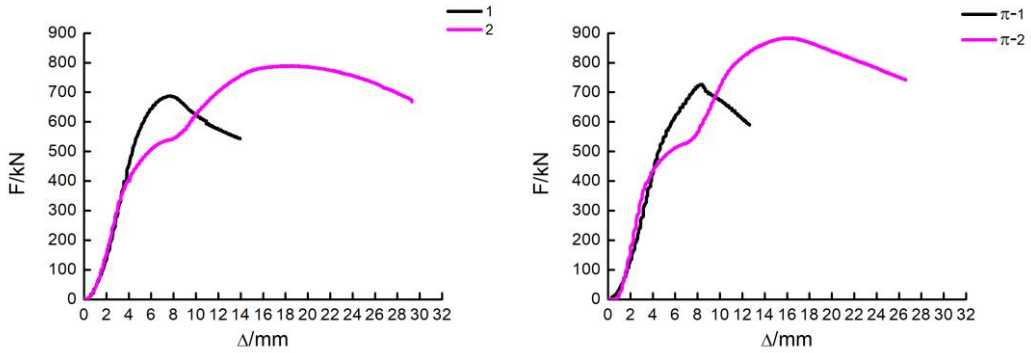
3.4 Axial load–axial curve

The measured axial load F–axial displacement Δ (F-Δ) curves of different beam–column joint specimens are shown in Figure 7. In particular, the comparison between measured F-Δ curves are shown in Figure 7(a) for bolted–welded joint specimens 1 and 5; in Figure 7(b) for π-shaped joint specimens π-1 and π-2; in Figure 7(c) for double L-shaped joint specimens with diagonal rib L-1 to L-5; in Figure 7(d) for CFST column joint specimens 1, π-1, and L-1; and in Fig. 7(e) for the H-shaped steel column joint specimens 2, π-2, and L-5.

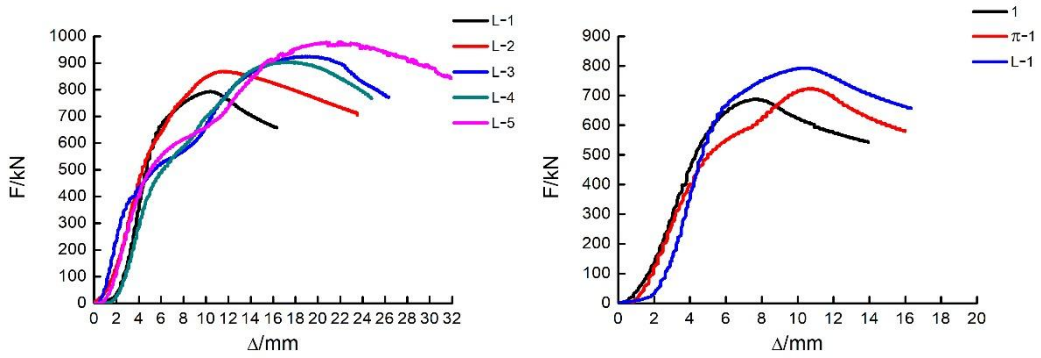
According to Figure 7(a)-(c), the 9 bolted–welded joint specimens basically maintain at the elastic deformation stage before the axial load reaches 450 kN. With the column height of the specimen at 448 mm, a measured mean value of 0.0016 for the yield strain ε_y of the steel plate with different thicknesses, and a strain of 0.016 for the specimen column at the end of the steel yield platform, the axial displacement of the specimen column at the end of the steel yield platform is 448 mm×0.016=7.168 mm, which is rounded to 7 mm. At this moment, obviously the axial deformation of the column has entered the yield deformation stage. Between the 9 specimens, specimen 2, π-2,L-2 is the H-shaped steel column, when the axial displacement is 7.168 mm, the stiffness and carrying capacity reachs the minimum. Compared to square steel columns,they have the largest elastic–plastic axial displacement, which is mainly caused by the buckling deformation of the H-shaped steel column flange . It is evident that excessive buckling deformation of the H-shaped steel column will be the key factor leading to collapse of the frame structure in an earthquake. Therefore, in the design of the bolted–welded beam–column joints of light steel frames, CFST columns should be used.

According to Figure 7(d), specimens 1, π-1, and L-1 are differently constructed joints of CFST columns. For the displacements when the F-Δ curves of the three specimens in the whole process reach peak load, specimen 1 has less displacement under peak load, while the displacements of specimens π-1 and L-1 approach each other and are significantly greater than that of specimen 1 under peak load. This is because with large joint areas for π-shaped joint specimen π-3 and double L-shaped specimen with diagonal rib L-1, slight damage has been caused after the low-frequency cyclic loading test is completed. When comparing the peak load of specimen π-1 and specimen L-1, the peak load of double-L-shaped specimens with diagonal ribs L-1 is obviously larger, so it shows that the joint performance of double-L-shaped specimens with diagonal ribs is the best.

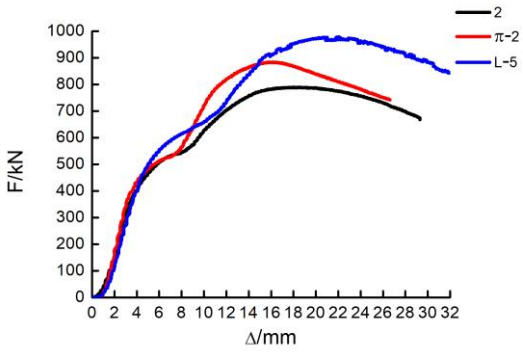
Figure 7(e) shows that specimens 2, π-2, and L-5 are differently constructed joints of H-shaped steel columns. When the axial displacements on the F-Δ curves of the three specimens in the whole process reach 4 mm, the specimen is at the restrained elastic–plastic deformation stage, and the corresponding mean strain is 4 mm/448 mm=0.0089, approximately 5.58 times the yield strain of the steel specimen, 0.0016. The test results show that the axial compression performance of L-5 specimens of double L-shaped connections with diagonal ribs is the best after low cycle repeated load test.



(a) F-Δ curves of bolted–welded joint (b) F-Δ curves of π-shaped joint



(c) F-Δ curves of double L-shaped joints with diagonal ribs (d) F-Δ curves for differently constructed joints of CFST columns



(e) F-Δ curves for differently constructed joints of H-shaped steel columns

Figure 7 Measured F-Δ Curves for Differently Constructed Beam–Column Joint Specimens

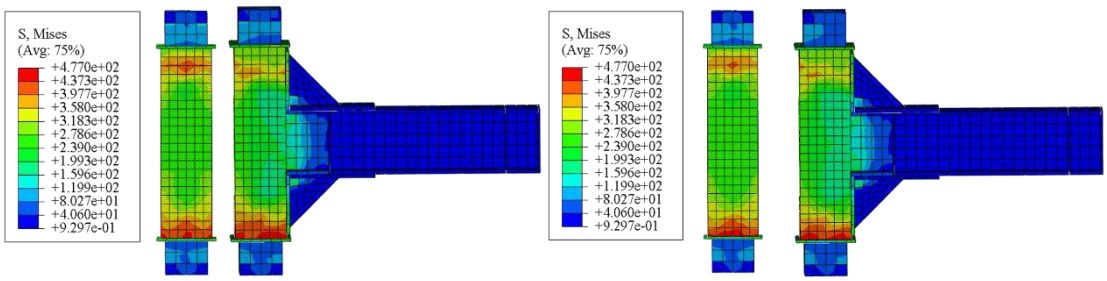
The measured axial characteristic deformation and characteristic load of each specimen are shown in Table 2. In the table, Fy is defined as the load at which the specimen has an axial displacement limit of 7 mm in restrained yield deformation, Δm is the peak displacement, Fm is the peak load, Δu is the failure displacement, and Fu is the failure load.

Table 2 Axial Characteristic Deformations and Characteristic Loads of Specimens

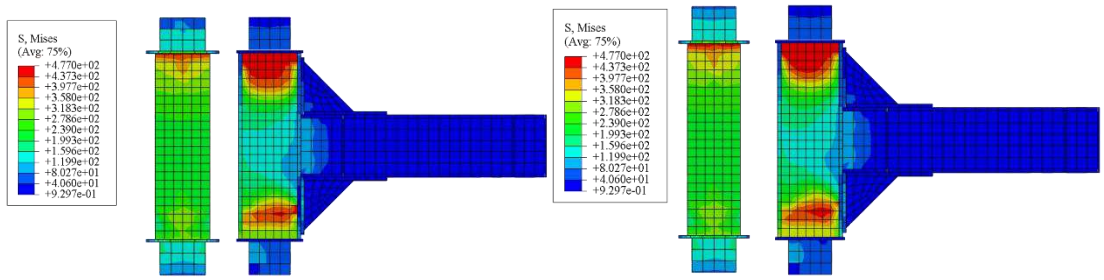
No.	Fy (kN)	Δm (mm)	Fm (kN)	Δu (mm)	Fu (kN)
1	580	8.36	679	13.44	550
2	535	18.36	788	29.31	665
π-1	603	8.26	725	12.65	590
π-2	525	15.86	883	26.62	730
L-1	674	10.45	792	16.33	650
L-2	700	11.95	866	23.53	703
L-3	567	19.28	922	26.81	932
L-4	558	18.50	900	24.82	750
L-5	554	23.78	965	33.87	800

3.5 Finite element calculation and analysis

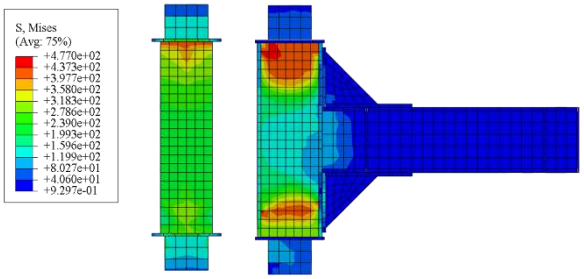
The finite element simulation results for the damage state of the five double L-shaped joints with diagonal ribs under axial compressive loads are shown in Figure 8. The L limbs of specimens L-1 to L-5 have different lengths and constructions. For specimens L-1 and L-2, when the loading displacement reaches 12 mm, the ends of the CFST columns are damaged. The stress maps are shown in Figure 8(a)-(b). For specimens L-3, L-4, and L-5, when the loading displacement reaches 30 mm, the H-shaped steel column ends are damaged. The stress maps are shown in Figure 8(c)-(e). For specimens L-1 to L-5, the ratios of the damaged area of the column side to the total area of the column side are 6.27%, 4.61%, 18.18%, 18.27%, and 15.46%, respectively. Thus, the larger the damaged area of the H-shaped steel column joint specimen, the more serious the damage. The calculated damage state fits well with the test result.



(a) Stress map of specimen L-1 (b) Stress map of specimen L-2



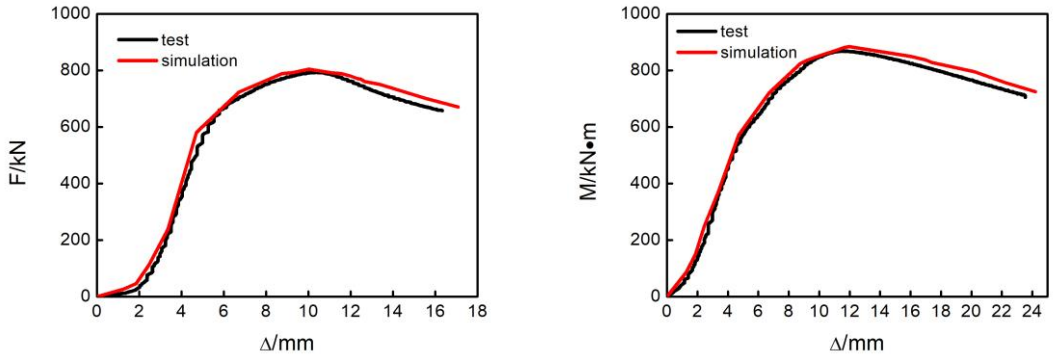
(c) Stress map of specimen L-3 (d) Stress map of specimen L-4



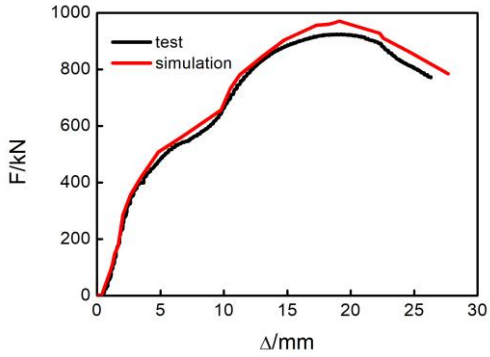
(e) Stress map of specimen L-5

Figure 8 Finite Element Simulation Results for Damage State of Double L-shaped Joint Specimens with Diagonal Rib under Axial Compressive Load

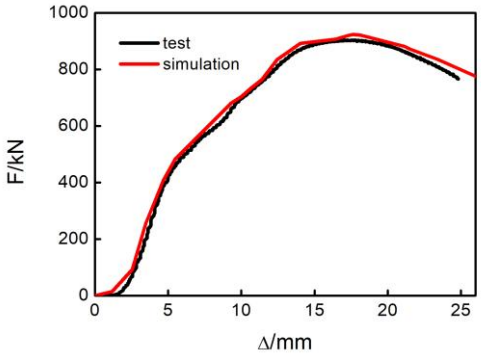
The comparison between finite element simulation of F-Δ curves and test results of five double L-shaped joint specimens with diagonal ribs is shown in Figure 9. The black lines are the test curves, and the red lines are the simulation curves. As shows, the calculated and test values of characteristic displacements and characteristic loads of the double L-shaped joint specimens with diagonal ribs. The minimum error between the simulated carrying capacity and the test result ranges from 1% to 9%.



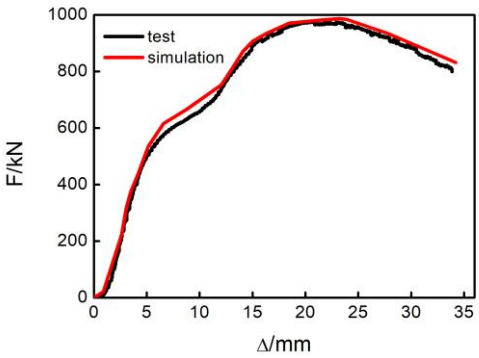
(a) Specimen L-1 (b) Specimen L-2



(a) Specimen L-3



(b) Specimen L-4



a wa

(e) Specimen L-5

Figure 9 Comparison between Finite Element Simulation of F-Δ Curves and Test Results of Double L-shaped Joint Specimens with Diagonal Ribs

4 Bearing capacity prediction model

To obtain the post-earthquake bearing capacity model of concrete-filled steel tubular columns with double L-shaped connections with diagonal ribs, we realized that we need to expand the number of data samples by changing the section size of the column, the strength of concrete or steel and other factors. Therefore, in section 3.4 of this paper, the test process of the specimen is restored through finite element modeling, and the results of the finite element model are consistent with the test results, with a small error. Therefore, this paper uses the finite element software to change the parameters of the test piece, and takes the finite element and test data as the composite data. We build the database of Gaussian regression process model with these 60 groups of data.

4.1 Machine learning method

4.1.1 Improved PSO Algorithm

Particle Swarm Optimization (PSO) was proposed by Dr. Eberhart and Dr. Kennedy in 1995[31]. The Particle Swarm Optimization (PSO) algorithm is an intelligent optimization technique inspired by the collective foraging behavior of bird flocks. Its objective is to locate the largest food source among multiple patches of varying sizes within a region, analogous to identifying the global optimum in an optimization problem. In PSO, each particle is defined by its position and velocity. Mimicking the adaptive search process of a flock, particles iteratively adjust their trajectories based on both individual experience and social information from the swarm. The velocity governs the direction and magnitude of movement, guiding the particles toward promising regions of the search space. Through successive iterations, the swarm converges toward the global optimal solution. The particle position and velocity are updated according to the following equations:

$$v_i^{t+1} = \omega v_i^t + c_1 r_1 (p_i^t - x_i^t) + c_2 r_2 (g_i^t - x_i^t) \quad (1)$$

$$x_i^{t+1} = x_i^t + v_i^{t+1} \quad (2)$$

Among them, v_i^t is the search speed of particle i, x_i^t is the position of particle i, p_i^t is the optimal position of particle i, g_i^t is the historical optimal position, t is the number of iterations, r_1 and r_2 are random numbers between [0,1], c_1 and c_2 are learning factors, and ω is the inertia factor.

For small datasets, insufficient samples hinder the exploration and exploitation capabilities of the particle swarm algorithm, causing particles to fall into local convergence during the search process. Consequently, the prediction accuracy of machine learning models becomes limited under small-sample conditions.

In performance-based criteria, the optimal values of particles and surrogate models with the best predicted fitness values are accurately evaluated in each iteration to control the search direction of the particle swarm. If the optimal value of the proxy model is better, the optimal value of the proxy model will replace the global optimal value of the current population. If only performance-based criteria are used, after several iterations, particles may concentrate in the optimal neighborhood of the model. Therefore, the group may quickly converge to a local optimum.

To achieve accuracy under small sample conditions, inspired by reference [47], this paper adopts uncertainty criteria to evaluate and determine the occurrence of local irrationality in the particle swarm update process based on the fitness function, and obtains the worst and best particle position distances. And SVM (Support Vector Machine) is used to predict new particle positions based on the optimal particle distance, thus forming a new particle population. Then, based on the performance evaluation indicators of the model, a prediction model with high accuracy under small sample conditions is obtained. The exploration process is shown in Figure 10.

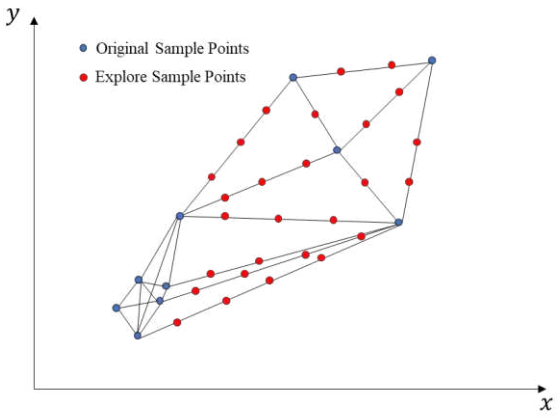


Figure 10 Plan view of particle swarm optimization exploration process based on SVM

The formula used during the exploration process is as follows:：

$$u_i = SVM(d_{norm,i}, \sigma_{norm,i}) \quad (3)$$

$$dm_i = \frac{1}{k}\sum_{j=1}^{k} d_{ij} \quad (4)$$

$$\sigma_i = \sqrt{\frac{1}{k}\sum_{j=1}^{k}(y_j - \bar{y})^2} \quad (5)$$

$$\bar{y} = \frac{1}{k}\sum_{j=1}^{k} y_j \quad (6)$$

$$dm_{norm,i} = dm_i / \sum_{i=1}^{N} dm_i \quad (7)$$

Among them, k is the number of nearest particles, d_{ij} is the distance from candidate i to the j-th nearest neighbor, σ_i is the fitness value calculated by the i-th nearest neighbor particle swarm, y_j represents the prediction of the j-th particle swarm, and SVM represents the prediction function using support vector machines.

4.1.2 GPR

In Gaussian processes, any point in the continuous input space is correlated with a random variable from a normal distribution, and any finite set of random variables satisfies a multivariate normal distribution. For example, any linear combination of variables follows a normal distribution, and the Gaussian process distribution is the joint distribution of all random variables in a continuous domain. Lazy learning methods are generally highly portable and applicable to different problem domains, but they require a large space to store the training dataset in real time. The lack of abstraction over the dataset leads to a large computational burden in the prediction process. Lazy classifiers are suitable for situations where the dataset has fewer features. Therefore, from the perspective of machine learning algorithms, Gaussian processes adopt a lazy learning approach to measure the similarity between samples, thereby predicting the outcome of positional observations based on training data. The prediction results are often marginal distributions

For a given dataset $D_N = [x_n, y_n]_{n-1}^{N}$, where $x_n \ni R$, let X=[x_1, x_2, …, x_n]denote the observed input data matrix, i.e., the input space. Y=[y_1, y_2, …, y_n] denotes the observed output vector, i.e., the output space. Consider a nonlinear mapping $\emptyset_{(x)}$: $x \ni R$, which may be unknown or of infinite dimension. Therefore, a kernel function is needed to construct the feature space. The kernel function is as follows:

$$K(x_i, x_j) = (\emptyset_{(x_i)}, \emptyset_{(x_j)}) \quad (8)$$

In the Gaussian regression model, each sample y_n can be represented as:

$$y = f(x) + \varepsilon \quad (9)$$

where f is a Gaussian process $f \sim N(0, K)$, $K = K(x_i, x_j)$ is a specific covariance matrix defined by the kernel function, and $\varepsilon \sim N(0, \sigma^2)$.

Define $K_{Xx} = [(K(x_1, x), \cdots K(x_N, x)]$. For any test data, estimate the predictive distribution. Based on the Gaussian probability assumption, the conditional distribution can be obtained:

$$p(y|x, X, Y) \sim N(f(x), g(x)) \quad (10)$$

Where：

$$f(x) = K_{Xx}^T (K + \sigma^2 \mathrm{I})^{-1} Y \quad (11)$$

$$g(x) = \sigma^2 + K(x, x) - K_{Xx}^T (K + \sigma^2 \mathrm{I})^{-1} K_{Xx} \quad (12)$$

Where I is the unit matrix of response scale.

4.2 Algorithm Implementation

The steps of the improved algorithm proposed in this paper are illustrated in Figure 11 and summarized as follows:

(1) Construct a model database : Establish a comprehensive database to serve as the foundational dataset for subsequent modeling and training.

(2) Select and apply appropriate machine learning algorithms – Implement suitable machine learning models, such as the GPR introduced in this study.

(3) Initialize model parameters using Particle Swarm Optimization (PSO): Incorporate the PSO algorithm to optimize the initial parameter settings, thereby improving efficiency and solution quality.

(4) Propose an improved GPR algorithm (IPSO-GPR): Modify the standard PSO framework according to the proposed improvements to strengthen its global search capability and prevent premature convergence to local optima.

(5) Develop a predictive model that meets accuracy requirements: Construct a refined predictive model that achieves high accuracy while adhering to physical consistency and real-world applicability.

4.3 Model performance evaluation

To evaluate the accuracy of the model, the following decision coefficient (R^2) is used to evaluate the performance of each model: its mathematical formula is as follows:

$$R^2 = 1 - \frac{\sum_{j=1}^{m} (\check{y}_j - y_j)^2}{\sum_{j=1}^{m} (\check{y}_j - \bar{y})^2} \quad (13)$$

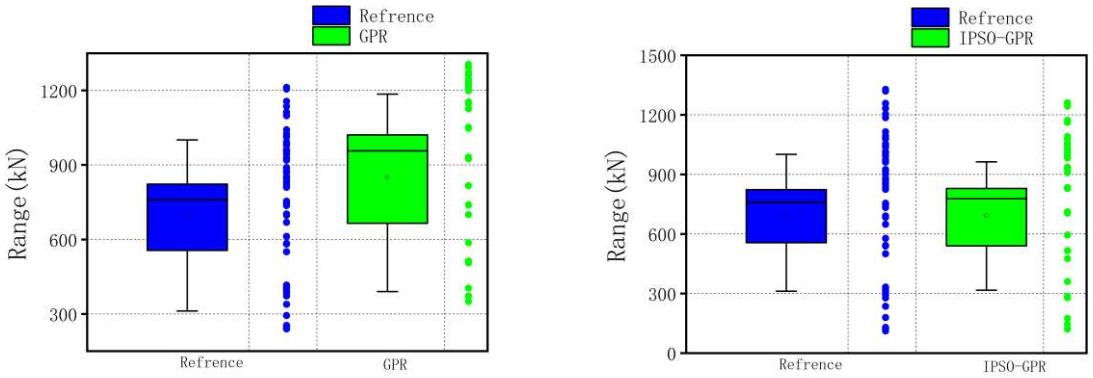
Where, $\check{y}_j$ J and y_j represents the predicted value and experimental value, m represents the total number of data, $\bar{y}$s the average of the test values. Theoretically, the R^2 value is between 0 and 1. When the model is close to 1, the better the prediction ability is, and when it is close to 0, the worse the prediction performance is. This performance indicator is a good measure of the overall prediction accuracy.

4.3 Model training and verification

In this study, the test dataset constructed in this paper was used as the modeling sample. First, probability distribution fitting tests were performed on each input variable. Based on K-S test and Q-Q plot analysis, the optimal distribution form was determined, and the corresponding distribution parameters were calculated using the maximum likelihood estimation method. Subsequently, a parameterized distribution model was employed to conduct Monte Carlo simulation, generating high-fidelity synthetic data that conform to actual statistical characteristics, thereby supporting subsequent model training and validation.

Figure 10 presents a box plot comparing the statistical distribution of bearing capacity prediction results using different methods. The vertical axis represents the bearing capacity values calculated from the measured and generated data. The box reflects the interquartile range of the predictions, while the scattered points indicate the distribution of outliers. Through visual comparison, it can be clearly observed that the improved IPSO-GPR method significantly outperforms the traditional Gaussian Process Regression (GPR) in terms of median position, upper limit (maximum value), and overall dispersion of the predictions. Moreover, its statistical characteristics show a higher consistency with the original data.

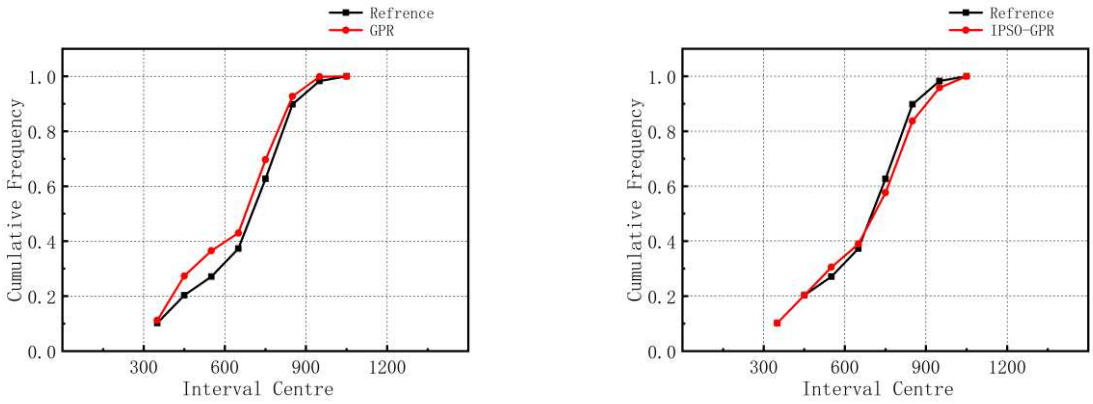
In terms of quantitative evaluation metrics, the IPSO-GPR model achieves a coefficient of determination R^2 of 0.97, indicating that the model can explain 97% of the variance in bearing capacity and demonstrates excellent goodness-of-fit. In contrast, the traditional GPR model only attains an R^2 of 0.83 on the same test set, revealing a clear limitation in its predictive capability. Additionally, by further calculating the Root Mean Square Error (RMSE) and Mean Absolute Percentage Error (MAPE), IPSO-GPR reduces these metrics by approximately 42% and 38%, respectively, compared to the baseline GPR. This further verifies the significant effectiveness of the proposed improvement strategy in enhancing the model's prediction accuracy and stability.



（a）GPR (b) IPSO-PSO

Figure 10 Box plot comparing the predicted values and actual values of the Gaussian regression process (b) probability distribution curve

Figure 11 presents a comparison between the cumulative distribution function (CDF) curve of the bearing capacity derived from the improved algorithm and that of the original dataset. The plot adopts a conventional CDF representation, with the horizontal axis indicating the parameter values (bearing capacity) and the vertical axis representing the corresponding cumulative probabilities. As can be observed, the CDF curve of the data generated by the improved IPSO-GPR algorithm closely aligns with the CDF of the original data, indicating a high degree of distributional consistency and validating the efficacy of the proposed enhancement in accurately preserving the statistical characteristics of the original bearing capacity distribution.



（a）GPR (b) IPSO-PSO

Figure 11 Probability distribution curve comparing the predicted values and actual values of the Gaussian regression process (b) probability distribution curve

4.4 Formula modifying

It is not convenient for engineers to use Gaussian regression process model in practice, because such models include covariance function and mean function In view of this, based on the results of GPR algorithm, we derive a practical prediction equation for the bearing capacity of concrete filled steel tubular columns with double L-shaped connections with diagonal ribs after earthquake.

In China, in order to effectively calculate the bearing capacity of concrete-filled steel tubular columns, the formula is proposed as follows [48]:

$$\mathrm{F} = f_c A_c (1 + t + \sqrt{t}) \qquad (13)$$

$$t = \frac{f_y A_s}{f_c A_c} \qquad (14)$$

In the above formula, f_c is the concrete strength value, A_c is the concrete section area, f_y is the steel strength value, A_s is the sectional area of the steel pipe.

Since the bearing capacity of concrete filled steel tubular columns with double L-shaped connections with diagonal ribs after earthquake in this paper is damaged after the main earthquake, the attenuation coefficient of bearing capacity is defined α。According to formula 2, the formula for calculating the bearing capacity of concrete-filled steel tube in the double-L-shaped joint area after earthquake is as follows:

$$\alpha = -0.78\beta^2 + 1.93\beta - 0.27 \qquad (15)$$

4.5 Formula validation

In order to visually observe the accuracy of the proposed formula and empirical formula, Fig. 12 shows the regression diagram between the calculated value of different formulas and the actual test value. It can be seen from Figure 11 that the calculated value of the proposed bearing capacity formula is in the highest consistency with the experimental value. In other words, the data

points of the ratio of the calculated value to the actual value are all around the function y=x, and the error is controlled within ± 10%. From the evaluation coefficient of the model, the R^2 value of the modified formula is 0.92, which is close to the ideal value of 1.

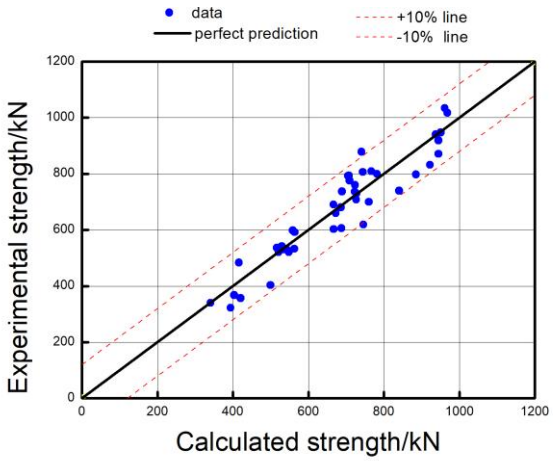


Figure 12 Comparison between the calculated value of the modified formula and the actual value

5 Conclusion

The vertical load-bearing capacity of earthquake-damaged prefabricated frame structures determines their ability to resist collapse during aftershocks, with the axial compression performance of the beam-column joint region after seismic damage playing a critical role in evaluating the structural vertical load-bearing capacity. To systematically investigate the load-bearing behavior of beam-column joints in post-earthquake prefabricated lightweight steel frames, this study first conducted axial compression performance tests on nine joints with varying degrees of damage and different structural configurations based on nine existing low-cycle reversed loading tests of beam-column joints in prefabricated lightweight steel frames. Axial forces were applied to the frame columns to compare the failure modes and load-bearing capacities of the joints. Subsequently, numerical simulations were performed to validate the experimental structures, and a database was established based on both experimental and finite element results. To further enhance prediction accuracy, an improved particle swarm optimization algorithm was employed to optimize Gaussian process regression, proposing the IPSO-GPR algorithm and developing a post-earthquake load-bearing capacity prediction method for lightweight steel frame structures.To accurately calculate the post-earthquake load-bearing capacity of concrete-filled steel tubular columns in beam-column joint zones with double L-shaped diagonal stiffeners, this study further established a load-bearing capacity prediction model based on experimental data and the finite element method. The main conclusions are as follows:

(1) The connection configuration of beam-column joints in prefabricated lightweight steel frames significantly affects their mechanical performance under low-cycle reversed loading. The load-bearing capacity of specimens with double L-shaped diagonal stiffeners was notably higher than that of the control group.

(2) The hysteretic curves of "beam-end moment M versus beam-column relative rotation angle θ" under low-cycle reversed loading and the "axial load F versus axial displacement Δ" relationships under axial compression, as obtained from finite element simulations, showed good agreement with experimental results. The deformation contour plots of concrete-filled steel tubular columns or H-shaped steel columns derived from simulations effectively reflected the damage evolution process of the specimens.

(3) Based on combined experimental and finite element simulation data, and considering the limitations of traditional empirical formulas in accurately characterizing the post-earthquake load-bearing capacity of specimens, a load-bearing capacity attenuation factor and a corresponding prediction model for component capacity were proposed. The model's predictions align well with experimental data, validating the effectiveness of the proposed method.

Funding：No

Consent to Publish declaration: not applicable

Consent to Participate declaration: not applicable

Ethics declaration: not applicable

Non clinical research

Data availablility :The data will be provided as required. Please contact the corresponding author.

Reference

[1] Xie, XY , Wang, D , Qian, YM .Summary of Research Status of Assembly Nodes.2019 international conference on advances in civil engineering, energy resources and environment engineering.2019,330.

[2] Cheng, D., Ma, J., & Iop. Research on the restrictive factors of the development of Chinese prefabricated buildings. Paper presented at the 3rd International Conference of Green Buildings and Environmental Management (GBEM), Electr Network.2020.

[3] Li, X., Wang, C., Alashwal, A., & Bora, S. Game analysis on prefabricated building evolution based on dynamic revenue risks in China. Journal of Cleaner Production.2020,267. doi:10.1016/j.jclepro.

[4] Lv, Z., Zhang, D., & Iop. Analysis of the life cycle stage of prefabricated buildings. Paper presented at the International Conference on Advances in Civil Engineering, Energy Resources and Environment Engineering (ACCESE), Jilin Jianzhu Univ, Coll Civil Engn, Changchun, PEOPLES R CHINA,2019.

[5] Navaratnam, S., Tuan, N., Gunawardena, T., & Henderson, D. Performance Review of Prefabricated Building Systems and Future Research in Australia. Buildings.2019,9(2). doi:10.3390/buildings9020038

[6] Wen, Y. Research on the intelligent construction of prefabricated building and personnel training based on BIM5D. Journal of Intelligent & Fuzzy Systems. 2021,40(4), 8033-8041. doi:10.3233/jifs-189625

[7] Yin, X., Huang, Q., Chen, P., Lin, L., & Feng, W. Carbon Emissions of Prefabricated Residential Building Based on Process Analysis Method. Paper presented at the International Conference on Construction and Real Estate Management (ICCREM), Beijing, PEOPLES R CHINA.2021.

[8] Nurchasanah, Y., Ujianto, M., Gagah, & Winoto, A.T.. Diagonal Reinforcement as Strengthening to Increase the Stiffness and Strength of Concrete Frame[J]. Advanced Science Letters, 2018,24(12), 9098-9103.

[9] Tang, B., Chen, S., Li, X., Xiong, L., Chen, H.-P., & Feng, Q.). Seismic performance of RC frames with EPSC latticed concrete infill walls. Engineering Structures[M], 2019,197. doi:10.1016/j.engstruct.2019.109437

[10] Arafa, M., Alqedra, M. A., & Salim, R.. Performance of RC Beams with Embedded Steel Trusses Using Nonlinear FEM Analysis[J]. Advances in Civil Engineering.2018, DOI10.1155/2018/9079818

[11] Jun, Ha Heon;Lee, Kangmin;오근영. Seismic Performance Evaluation of Reinforced Concrete Frames Reinforced with Chevron Bracing System[J]. Journal of The Korea Institute for Structural Maintenance and Inspection.2018,22,13-22.

[12] Chalioris, C. E., & Bantilas, K. E. Shear strength of reinforced concrete beam-column joints with crossed inclined bars[J]. Engineering Structures, 2017,140, 241-255.

[13] Iqbal, A., Pampanin, S., & Buchanan, A. H.. Seismic Performance of Full-Scale Post-Tensioned Timber Beam-Column Connections. Journal of Earthquake Engineering.2016, 20(3), 383-405. doi:10.1080/13632469.2015.1070386

[14] Li, Y., & Huang, B. Research on load-bearing performance of new fabricated steel structure beam-column joints with energydissipating elements. Structures, 38, 492-501. doi:10.1016/j.istruc.2022.02.001

[15] Liu Xuechun ; Yang Zhiwe; Wang Hexiang ea al. Seismic performance of beam-column connection in bolted assembled multi-high-rise steel structure. Journal of Building Structures.2017,38(6): 34-42.（in chinese）

[16] Li, DB, Wu, CX , Zhou, Y.A precast beam-column connection using metallic damper as connector: Experiment and application. JOURNAL OF CONSTRUCTIONAL STEEL RESEARCH. 2021,181.DOI10.1016/j.jcsr.2021.106628.

[17] Rajagopal, S,Prabavathy, S. Study of exterior beam-column joint with different joint core and anchorage details under reversal loading. STRUCTURAL ENGINEERING AND MECHANICS.2013,46(6):809-825.

[18] Han, C ,Li, QN , Wang, X . Research on rotation capacity of the new precast concrete assemble beam-column joints. STEEL AND COMPOSITE STRUCTURES.2016,22(3):613-625. DOI10.12989/scs.2016.22.3.613.

[19] Ma, CL,Jiang, HB , Wang, ZY .Experimental investigation of precast RC interior beam-column-slab joints with grouted spiral-confined lap connection. ENGINEERING STRUCTURES.2019,196. DOI10.1016/j.engstruct.2019.109317.

[20] Korkmaz H H and Tankut T . Performance of a precast concrete beam-to-beam connection subject to reversed cyclic loading Engineering Structures ,2005,27(9): 1392-1407.

[21] Zhou Y, Wu H and Gu A Q. Earthquake engineering: from earthquake resistance, energy dissipation, and isolation to resilience [J]. Engineering Mechanics; 2019,36(06):1-12.

[22] Christopoulos C, Montgomery M S. “Viscoelastic coupling dampers (VCDs) for enhanced wind and seismic performance of high-rise buildings ”. Earthquake Engineering & Structural Dynamics,.2013,42(15):2217—2233.

[23] Wang Meng, Ke Xiaogang, Wu Zhaozhang .seismic behavior of steel frame connections with replaceable high ductility and energy dissipation components. Engineering Mechanics.2018,35(12):151-163.

[24] Lin X, Kato M, Zhang L, Nakashima M. Quantitative investigation on collapse margin of steel high-rise buildings subjected to extremely severe earthquakes. Earthq Eng Eng Vib 2018;17(3):445–57.

[25] Li, S., Liu, G., & Zhao, D. Replaceable prefabricated concrete-filled steel tubular node. Ceramics-Silikaty, 2022,66(3), 335-348. doi:10.13168/cs.2022.0026

[26] Liu, Y., Wang, X., & Shi, Q. . Experimental Study on K-type Eccentrically Braced Steel Frame with Replaceable Links.. Progress in Steel Building Structures, 2021,,23(6), 30-35,60. (in Chinese)

[27] Xue, G., Bao, W., Jiang, J., & Shao, Y. Hysteretic Behavior of Beam-to-Column Joints with Cast Steel Connectors. Shock and Vibration, 2019. doi:10.1155/2019/9802672

[28] Zhang, AL , Wang, HW, Jiang, ZQ. Numerical simulation analysis of double yield points assembled buckling-restrained brace with replaceable inner core. STRUCTURES.2022,35:1278-1294. DOI10.1016/j.istruc.2021.09.061

[29] Wang, D , Xiao, XF, Yan, GY. Seismic Performance of Assembled Buckling-Restrained Braced Frame Structure with Replaceable Plasticity-deformation Controllable Steel Hinges. 2020 4TH INTERNATIONAL WORKSHOP ON RENEWABLE ENERGY AND DEVELOPMENT .2020,510. DOI10.1088/1755-1315/510/5/052036.

[30] LU X L，CUI Y，LIU J J，GAO W J． “Shaking table test and numerical simulation of a 1 /2-scale self centering reinforced concrete frame”． Earthquake Engineering ＆ Structural Dynamics. 2015,44 (12) :1899-1917．

[31] Lu X , Chen C , Chen Y , et al. “Application of replaceable coupling beams to RC structures: Application of Replaceable Coupling Beams”. The Structural Design of Tall and Special Buildings, 2016,25(17):947-966.DOI:10.1002/tal.1292

[32] Eftimie, F.. THE STUDY BEHAVIOUR OF MULTISTORY BUILDINGS WITH DUAL METALLIC FRAMES. Paper presented at the International Conference on Military Technologies (ICMP 2007), Univ Def, Fac Mil Technol, Brno, CZECH REPUBLIC.

[33] Takeya, K., Fuse, T., Kinoshita, H., & Parker, N. W.Simulation of robustness of a new e-beam column with the 3(rd)-order imaging technique. Paper presented at the Conference on Emerging Lithographic Technologies XII, San Jose, CA. 2008,Feb 26-28

[34] Wang, F.-e. Frame beam-column joints in the design of the concrete strength grade. Paper presented at the 3rd International Conference on Civil, Architectural and Hydraulic Engineering (ICCAHE), Hangzhou, PEOPLES R CHINA. 2014, Jul 30-31

[35] Jia, S.; Cao, W.; Zhang, Y. Low reversed cyclic loading tests for integrated precast structure of lightweight wall with single row reinforcement under a lightweight steel frame. R. Soc. Open Sci. 2018, 5, 180321. https://doi.org/10.1098/rsos.180321

[36] Yao, Y., Chu, Y., Zhang, Z., & Deng, Y. Experimental research on seismic behavior of beam-column nodes with concrete filled cold-formed thin-walled square steel tubes. Building Structure, 2013,43(22), 1-4,8.（in chinese）

[37]Guo, X., Wang, Q., Shu, Y., Zhou, H., & Iop. The Seismic Performance Study on Composite Concrete-Filled Steel Tube Column-Steel Beam Node. Paper presented at the 4th International Conference on Environmental Science and Material Application (ESMA), Xian, PEOPLES R CHINA. 2019,Dec 15-16.

[38] Ding Wei,Jia Suizi. Numerical Investigation of the Seismic Performance of Steel Frames with Energy-Dissipating Composite Walls. MATERIALS.2022,15(3). DOI10.3390/ma15030828.

[39] Ben Chaabene, W., Flah, M., & Nehdi, M. L.. Machine learning prediction of mechanical properties of concrete: Critical review. Construction and Building Materials, 2020.260. doi:10.1016/j.conbuildmat.2020.119889

[40] Zhang, W., Lee, D., Lee, J., & Lee, C. Residual strength of concrete subjected to fatigue based on machine learning technique. Structural Concrete, 2022,23(4), 2274-2287. doi:10.1002/suco.202100082

[41] Solhmirzaei, R., Salehi, H., & Kodur, V. Predicting Flexural Capacity of Ultrahigh-Performance Concrete Beams: Machine Learning-Based Approach. Journal of Structural Engineering, 2022,148(5). doi:10.1061/(asce)st.1943-541x.0003320

[42] Thirumalaiselvi, A., Verma, M., Anandavalli, N., & Rajasankar, J. Response prediction of laced steel-concrete composite beams using machine learning algorithms. Structural Engineering and Mechanics, 2018,66(3), 399-409. doi:10.12989/sem.2018.66.3.399

[43] Tien-Thinh Le. Practical Hybrid Machine Learning Approach for Estimation of Ultimate Load of Elliptical Concrete-Filled Steel Tubular Columns under Axial Loading. Advances in Civil Engineering.2020.

[44] Wen, Y. Research on the intelligent construction of prefabricated building and personnel training based on BIM5D. Journal of Intelligent & Fuzzy Systems. 2021,40(4), 8033-8041. doi:10.3233/jifs-189625

[45] Rajagopal, S,Prabavathy, S. Study of exterior beam-column joint with different joint core and anchorage details under reversal loading. STRUCTURAL ENGINEERING AND MECHANICS.2013,46(6):809-825

[46] Xue, G., Bao, W., Jiang, J., & Shao, Y. Hysteretic Behavior of Beam-to-Column Joints with Cast Steel Connectors. Shock and Vibration, 2019. doi:10.1155/2019/9802672

[47] A new optimizer using particle swarm theory, in: MHS'95. Proceedings of the Sixth International Symposium on Micro Machine and Human Science, Ieee, 1995, pp. 39-43..

[48] China Association For Engineering Construction Standardization. CECS ;Specification For Design And Construction Of Cnocrete-Filled Steel Tybular Structures. 1991, Beijing.